Probing the structural transition from buffer layer to quasifreestanding monolayer graphene by Raman spectroscopy

S. Wundrack,[1] D. Momeni Pakdehi,[1] P. Schädlich,[2] F. Speck,[2] K. Pierz,[1] T. Seyller,[2] H. W. Schumacher,[1] A. Bakin,[3,4] and R. Stosch[1]

[1]*Physikalisch-Technische Bundesanstalt, Bundesallee 100, D-38116 Braunschweig, Germany*
[2]*Institut für Physik, Technische Universität Chemnitz, Reichenhainer Straße 70, D-09126 Chemnitz, Germany*
[3]*Institut für Halbleitertechnik, TU Braunschweig, Hans-Sommer Straße 66, D-38106 Braunschweig, Germany*
[4]*Laboratory of Emerging Nanometrology (LENA), TU Braunschweig, Hans-Sommer Straße 66, D-38116 Braunschweig, Germany*

(Received 23 July 2018; revised manuscript received 15 October 2018; published 30 January 2019)

The structural transition of a graphene buffer layer epitaxially grown on 6*H* silicon carbide (SiC) to quasifreestanding monolayer graphene by intercalation of oxygen and water molecules at low concentrations is studied by temperature-dependent Raman spectroscopy. We present a detailed investigation of the defect density and strain and doping evolution in the graphene crystal lattice. The structural transition from the buffer layer to monolayer graphene with high defect densities occurs at temperatures from 400 to 500 °C, revealing the nanocrystalline regime of stage 2 of the amorphization trajectory, followed by the transition into stage 1 as evidenced by a gradual reduction of defects in graphene during subsequent annealing up to 900 °C.

DOI: 10.1103/PhysRevB.99.045443

I. INTRODUCTION

Graphene provides remarkable electrical transport properties as well as an outstanding quantum Hall effect, caused by its sp^2-hybridized bonding state resulting in a delocalized electron system across the entire carbon crystal lattice [1–4]. Therefore, the fabrication of large-area high-quality graphene is still an ongoing research topic that opens up new fields of electronic applications as well as for resistance and impedance standards in metrology [5–9]. The formation of large-area graphene has been achieved among others by chemical vapor deposition (CVD) [10–13] as a top-down growth process or the pyrolysis of large carbon nanomembranes based on the electron irradiation-induced crosslinking of self-assembled monolayers [14–17] as well as by epitaxial growth on different polytypes of silicon carbide (SiC) [18–21]. The latter technique especially appears to be very promising as it enables monolayer graphene to be formed directly on a semi-insulating 6*H*- or 4*H*-SiC substrate without the need for additional transfer to semiconducting substrates for further electronic device fabrication. When graphene is grown on the silicon-terminated SiC(0001) surface, the so-called buffer layer is formed at the interface, a layer of carbon atoms in graphenelike arrangement devoid of graphene's characteristic electronic properties since it is in part covalently bound to the SiC [22]. Recently, the graphene buffer layer growth on the SiC substrate has been significantly improved by using the polymer-assisted growth of graphene (PASG) technique promoting the buffer layer nucleation by depositing an additional carbon source on 6*H*- or 4*H*-SiC substrates [18]. This technique notably improved the buffer layer coverage and thus the structural quality of epitaxial graphene, which is highly demanded for commercial graphene fabrication at the centimeter scale. Unfortunately, the presence of the buffer layer as well as unsaturated dangling bonds from the SiC substrate introduce charge transfer into the graphene monolayer [23,24]. This reduces the high carrier mobility of graphene which finally results in noticeable degradation of the electrical properties [25,26]. Hence, the detachment of the buffer layer from the SiC substrate induced by intercalation is one of the promising techniques to avoid such strong interactions. Furthermore, decoupling and subsequent conversion of the buffer layer into a graphene monolayer from the substrate is beneficial since the lattice parameter mismatch as well as the different thermal expansion coefficients of the two adjacent materials generally introduce strain in the graphene crystal lattice [27–31]. A transition from the insulating electronic properties of the buffer layer into a zero-band-gap quasifreestanding monolayer graphene (QFMLG) by intercalation of hydrogen as well as by the intercalation of lithium has been demonstrated [32–35]. The former intercalation process predominantly breaks the chemical bonds between the buffer layer and SiC and subsequently saturates and passivates the unsaturated dangling bonds of the substrate [26,33] leading to a carrier-type inversion in QFMLG [23,26,36] in comparison with regular graphene monolayer on top of the buffer layer. Another effective intercalation of the buffer layer has been achieved using molecular oxygen, air, or water as the intercalating agent [37–42]. At the same time, the passivation of the SiC surface due to the presence of a thin silicon oxide layer has been proved [37–42]. However, changes in phonon properties of the buffer layer and the freestanding graphene layer during such temperature-dependent intercalation process have not yet been monitored by Raman spectroscopy.

In this work, we investigate by means of confocal Raman spectroscopy the structural transition from buffer layer to quasifreestanding monolayer graphene in a nitrogen atmosphere containing low impurity concentrations of oxygen and

water molecules. We also evaluate the change in phonon properties of the buffer layer and graphene to estimate the type of defects, strain, as well as doping effects. We show that Raman spectroscopic data are in good agreement with previously published intercalation results and that Raman spectroscopy can be used for providing deeper insights into the mechanism and for more precisely controlling the intercalation process of the buffer layer. Finally, we prove that low oxygen and water contents also enable the conversion of the buffer layer into QFMLG containing low-level defect densities.

II. MATERIALS AND METHODS

The buffer layer was grown on the silicon face of samples (5×10) mm² cut from a semi-insulating 6*H*-SiC wafer with a nominal miscut angle of about 0.06° toward the [1$\bar{1}$00] surface. The samples were prepared according to the PASG technique [18,43], which involves polymer adsorbates to be formed on the SiC surface by liquid-phase deposition from a diluted solution of photoresist (AZ5214E) in isopropanol followed by sonication and final rinsing with isopropanol. The buffer layer growth was performed at 1400 °C (1 bar, 30 min) with a pre-vacuum-annealing at 900 °C [43]. Prior to each intercalation step the furnace and the sample were preannealed in vacuum at ∼450 °C to remove residues of adsorbed oxygen or water molecules from the furnace as well as from the sample surface. The temperature-dependent intercalation of the buffer layer was carried out in a nitrogen atmosphere (5N purity, ∼1 bar), containing an impurity concentration of oxygen and water of at least ∼4 ppm. Although we have carefully checked the furnace for gas leaks to avoid contaminations from air, we cannot totally exclude additional impurity sources, e.g., adsorbed residues of oxygen and water molecules on the furnace wall and thus possibly raising the impurity concentration of oxygen and water molecules into a slightly higher ppm regime. Furthermore, the intercalation of the buffer layer was performed at 100 °C and from 400 to 900 °C with temperature increments of 100 °C. After each annealing step the sample was removed from the furnace and subsequently characterized by Raman spectroscopy. Confocal micro-Raman mappings were acquired at ambient conditions with a LabRAM Aramis Raman spectrometer (Horiba) equipped with a 600 grooves mm^{-1} holographic grating, a frequency-doubled Nd:yttrium-aluminum-garnet laser emitting at 532 nm ($E_L = 2.33$ eV), and a 100× (NA 0.9) objective to focus the excitation laser onto the sample surface. Surface Raman mapping images were recorded over (20×20) µm² scan areas in backscattering mode using a piezo-driven xy-stage (PI) and a scanning step size of 0.1 μm. Complementary x-ray photoelectron spectroscopy (XPS) measurements were performed using monochromatic Al K_α radiation (1486.6 eV) and a hemispherical Phoibos 150 MCD-9 analyzer (SPECS). Prior to XPS, samples were degassed at a maximum temperature of ∼370 °C which was held for 1 h.

III. RESULTS AND DISCUSSION

Stepwise heating of the buffer layer sample grown on 6*H*-SiC (0001) from room temperature up to 900 °C in a static nitrogen atmosphere containing low impurity concentrations of oxygen and water results in a gradual transition to QFMLG which has been monitored by confocal Raman spectroscopy shown in Fig. 1. Due to the spectral superposition of the second-order vibrational modes of 6*H*-SiC and the phonon modes of graphene, all Raman spectra were corrected by subtracting spectra obtained from a pure 6*H*-SiC reference sample [31]. In addition, Raman mappings were recorded after each intercalation step. These spectra have been evaluated in terms of characteristic peak parameters such as peak position and peak width using a nonlinear curve-fitting algorithm. The mean values of these quantities are summarized in Fig. 2 with the error bars representing the associated standard deviations, whereas detailed values of the peak positions and peak widths can be found in the Supplemental Material [44]. Areas marked in gray and white indicate temperature ranges in which the phonon modes can be clearly assigned to buffer layer and QFMLG, respectively, whereas the dark-gray area indicates the range of transition from buffer layer to QFMLG. The Raman spectrum obtained at 25 °C as shown in Fig. 1(a) corresponds to a typical buffer layer involving three phonon bands at ∼1390, ∼1495, and ∼1605 cm^{-1} related to the center of gravity of the Raman bands. The phonon bands of the buffer layer can normally be deconvoluted by using four Lorentzian functions [45]. In contrast to literature data, the nonsymmetric band shape observed between 1200 and 1400 cm^{-1} required five Lorentzian functions to be considered in nonlinear curve-fitting. Since there is no classification of the buffer layer phonons elsewhere, we denote the peaks identified in this experiment as $^*D_1$, $^*D_2$, $^*G_1$, $^*G_2$, and $^*G_3$ of the buffer layer [Fig. 1(b)]. This labeling is not related to any irreducible representation of the underlying point-group symmetry. The phonon-dispersion behavior of the buffer layer as calculated by Fromm *et al.* has revealed a clear difference from the typical phonon-dispersion behavior of graphene due to the chemical bonding of the buffer layer to the SiC surface [45]. Furthermore, Fromm *et al.* suggested that there is a considerable backfolding of the phonon dispersion of the buffer layer onto the Γ point in the Brillouin zone resulting from a relatively small reciprocal unit cell of the buffer layer [45]. Hence, the Raman spectrum of the buffer layer and, thus, the $^*D_1$, $^*D_2$, $^*G_1$, $^*G_2$, and $^*G_3$ phonon bands correspond rather to vibrational density of states than to discrete phonon peaks [45]. In addition, the subtraction routine from a pure 6*H*-SiC reference sample reduces the signal-to-noise ratio in the acquired Raman spectrum. It may also introduce spectral artifacts also known as "wiggles" arising somewhat above 1500 cm^{-1}, triggered by a slight spectral mismatch (<1 cm^{-1}) between the two Raman spectra probably resulting from uncertainties in Raman spectral calibration. Consequently, this procedure might affect the subsequent evaluation of phonon properties especially of the $^*G_1$ phonon mode, introducing a slightly increased uncertainty. A prominent feature of the buffer layer is the broadened and flattened band shape compared to phonon modes of graphene, which is most likely caused by the presence of covalent bonds between silicon and carbon atoms as schematically shown in Fig. 1(c) (25 °C). These Si–C bonds change the electronic structure and the phonon-dispersion behavior of the graphene layer and lead to the absence of the Kohn anomaly as stated by Fromm *et al.* [24]. Furthermore, no 2*D* peak appears in the Raman

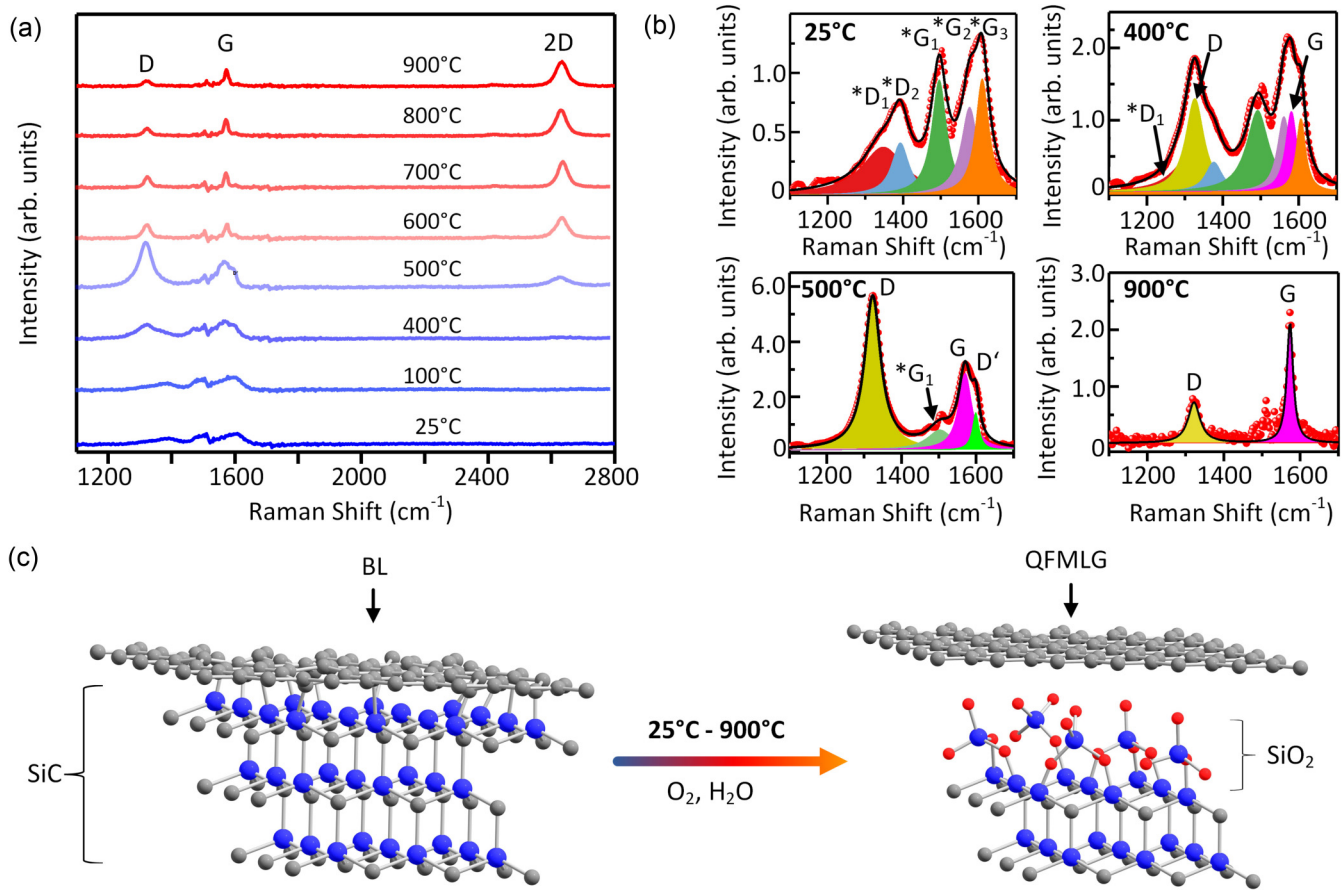

FIG. 1. (a) Raman spectroscopic monitoring of the transition of buffer layer to QFMLG at different temperatures. (b) Nonlinear curve-fitting of the spectra from graphene buffer layer and QFMLG at different annealing temperatures. (c) Schematic representation of buffer layer intercalation from 25 to 900 °C.

spectrum, which denotes another characteristic feature in the Raman spectroscopic fingerprint of the buffer layer. Generally, the 2*D* peak designates the double-resonance electron-phonon scattering process and is referred to as an overtone in the graphene Raman spectrum [46]. The Raman spectrum of the buffer layer shown in Fig. 1(a) as well as the evaluation of the buffer layer phonon modes with respect to peak position and peak width in Figs. 2(a) and 2(b) do not show any characteristic change at 100 °C, indicating an intact buffer layer crystal lattice existing at this step. Raising the annealing temperature up to 400 °C noticeably changes the Raman spectrum, which is predominantly indicated by a spectral softening of almost all phonon bands of the buffer layer [Fig. 2(a)], thus implying slight structural changes of the buffer layer lattice, which could probably be attributed to the gradual disappearance of the phonon-dispersion behavior of the buffer layer resulting from the steady conversion into QFMLG. Moreover, Fig. 1(b) shows the rise of the *D* and *G* peaks in the Raman spectrum of the buffer layer at 400 °C, indicating the start of the lattice transformation from the buffer layer into QFMLG as schematically depicted in Fig. 1(c). In this context, the *G* peak corresponds to the doubly degenerate E_{2g} phonon mode at the Γ point in the Brillouin zone [46]. The *D* peak is related to a forbidden phonon mode in pristine graphene, but it is activated in the presence of symmetry-breaking lattice effects such as point defects, grain boundaries, or substitutional doping [47–51]. This single-degenerate A_{1g} phonon mode is also related to an in-plane ring breathing phonon mode and its appearance indicates the presence of sp^2-hybridized carbon rings [52,53]. The further increase to an annealing temperature of 500 °C results in an increased *D* peak intensity and the simultaneous appearance of the 2*D* peak, emphasizing the spectral superposition of QFMLG and buffer layer phonon modes in the Raman spectrum [Fig. 1(b)]. However, it is known that both etching and oxidation processes of graphene layers may also cause a change in the *D* peak intensity [54–56] and should be considered as well, but will be discussed later. Since the characteristic spectral fingerprint of QFMLG appears in the Raman spectrum at ∼500 °C containing the typical *D*-, *G*-, and 2*D* peak of graphene (∼1323, ∼1571, and ∼2643 cm^{-1}) we can also assign the so-called *D*′ peak as an additional phonon mode occurring as a small shoulder around ∼1601 cm^{-1} [Fig. 1(b)]. Interestingly, $^*G_3$ and *D*′ peaks occur in a similar spectral range, potentially indicating that both peaks belong to the same irreducible representation. The *D*′ phonon mode is activated by a single-phonon intravalley scattering process and especially the D/D' intensity ratio can be used to determine the type of lattice defects in the graphene layer [48,57]. The intercalation process of the buffer layer in the temperature range from 500 to 700 °C leads to a visible sharpening and hardening of the phonon peaks of QFMLG [Figs. 2(a) and 2(b)]. The *G* (2*D*) peak

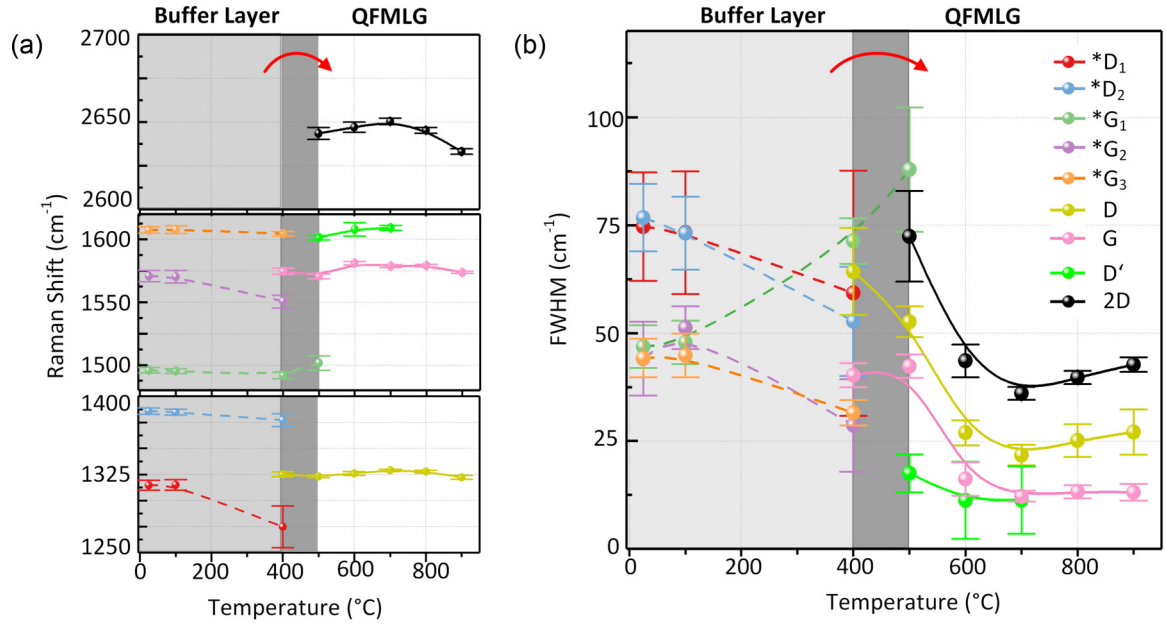

FIG. 2. (a) Evolution of the peak positions and (b) peak widths of the fitted buffer layer and graphene phonon modes during the intercalation process. The lines are guides to the eye.

width of ∼16(∼44) cm^{-1} as well as the G ($2D$) peak position of about ∼1581(∼2647) cm^{-1} clearly shows typical Raman features of QFMLG even at an annealing temperature of 600 °C. Upon further temperature increase up to 700 °C, the phonon hardening of the D, G, and $2D$ peaks reaches its maximum [Fig. 2(a)]. In this context, the temperature increases of 200° C noticeably change the positions of the D, G, and $2D$ peaks by about ∼5, ∼9, and ∼7 cm^{-1}, respectively. Finally, after finishing the annealing sequence at 900 °C, the Raman spectrum [Figs. 1(a) and 1(b)] resembles that of graphene, while the $2D$ peak width of ∼40 cm^{-1} clearly denotes the presence of QFMLG [Fig. 2(b)] [30,40]. A phonon softening of the D, G, and $2D$ peaks arises above 700 °C. The final positions of these peaks at 900 °C were found to be ∼1322, ∼1574, and ∼2633 cm^{-1}, respectively, which clearly differs from the phonon peak positions typically obtained for exfoliated graphene on SiO_2 [58–60]. Besides the phonon softening that occurs during the intercalation process, we also noticed a significant change of the D peak intensity at different annealing temperatures which is related to the alteration of defect densities introduced into the graphene crystal lattice. It is obvious that the D peak intensity steadily decreases during the intercalation process between 500 and to 900 °C, revealing a declining number of point defects in the graphene lattice, which can likely be attributed to an increasing annealing temperature, but possibly also to the continuously increasing duration of the intercalation procedure. The behavior of the D peak intensity at certain defect density levels has been extensively investigated by Cançado *et al.* [47], who applied argon ions at different ion doses to a graphene sample. As a result, they were able to quantify the point-defect density in graphene from values of the D/G intensity ratio. Furthermore, the combination of D/G intensity ratio and the G peak width enables the discrimination between stage 1 and stage 2 within the amorphization trajectory [47,53,61]. Here, we used this intensity ratio to quantify the defect densities by evaluating the Raman mappings obtained after different steps of the intercalation process. The false color images generated from these data indicate a declining defect density in the QFMLG during the intercalation process [Fig. 3(a)]. The highest defect density was observed to occur at 500 °C, and is undoubtedly larger than $\sim 3 \times 10^{12}$ cm^{-2} as demonstrated by a broad G peak width of (42.4 ± 2.8) cm^{-1} as well as a D/G intensity ratio of ∼2, indicating the stage 2 nanocrystalline regime within the amorphization trajectory [47]. It is important to note that the color scalebar for n_D [Fig. 3(a)] is limited to only 5×10^{11} cm^{-2} to preserve the color contrast of this image. Furthermore, this evidence is being underpinned by the G peak position of (1570.6 ± 1.9) cm^{-1} and by the broad $2D$ peak width of (72.4 ± 10.5) cm^{-1} [47,53,61]. The defect density continuously reduces down to $(0.8 \pm 0.1) \times 10^{11}$ cm^{-2} while the intercalation steadily progresses from 500 to 900 °C, revealing the transition into a stage 1 regime within the trajectory, which is confirmed by the sharpening of the G peak width below 20 cm^{-1} at 600 °C [47]. While the most heterogeneous pattern occurs especially at 500 and 600 °C possibly resulting from a nonhomogeneous intercalation process as well as from local hot spots of defect densities, this effect is significantly reduced at temperatures of 700 °C and above, indicating the improvement of the structural lattice quality during the intercalation process. Similar results were presented by Robinson *et al.* [62], who investigated the elimination of the buffer layer in epitaxial graphene by hydrogen intercalation. Another parameter to be derived from graphene Raman spectra is the D/D' intensity ratio enabling the defect types in the graphene crystal to be determined. Eckmann *et al.* have demonstrated that the D/D' intensity ratio reaches its maximum of ∼13 for sp^3 defects, drops down to ∼7 in the presence of vacancies, and reaches a minimum of ∼3.5 for grain boundaries [48,63]. From our data we

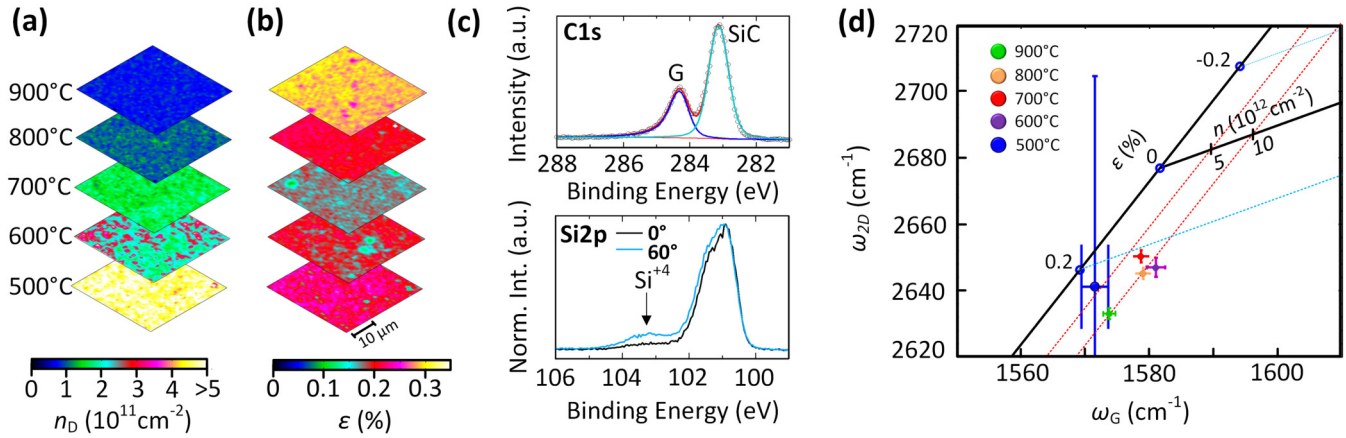

FIG. 3. Images generated from Raman mapping data showing (a) defect density clearly above 5×10^{11} cm^{-2} at 500 °C indicating stage 2 regime as well as defect densities below $\sim 4 \times 10^{11}$ cm^{-2} related to a temperature range from 600 to 900 °C, (b) strain distribution during the intercalation process in QFMLG, (c) XPS spectra of the C 1s and Si 2p core levels after the intercalation process at 900 °C, and (d) strain-doping trajectory related to the stepwise buffer layer intercalation.

have calculated D/D' values of (5.2 ± 1.0) at 500 °C and (5.7 ± 2.6) at 600 °C, respectively, which are comparable to data of the buffer layer intercalation using water vapor from Ostler *et al.* [41]. Although both values are associated with large standard deviations implying defect fluctuations, they are clearly below the threshold indicating the presence of sp^3-type defect regimes. However, the former D/D' value at an annealing temperature of 500 °C could be erroneous probably due to the appearance of high defect concentrations in the stage 2 regime so the information about the defect types is lost [48,63]. Rather, the calculated D/D' ratio at 600 °C presumably suggests a regime of vacancy-type defects as well as grain boundaries in the QFMLG related to partial intercalation at the beginning of the intercalation.

Graphene etching and graphene oxidation during buffer layer intercalation are additional effects that can considerably affect the defect density inside the carbon crystal lattice, and thus need to be considered here. Several research groups have investigated the bonding state of carbon in quasifreestanding graphene on SiC prepared by annealing in an oxygen atmosphere, in air as well as water-containing atmosphere using XPS [37–42]. No oxygen species bound to carbon atoms could be derived from the XPS data that would reveal a defective graphene layer, and thus graphene oxidation. However, XPS has shown the appearance of an ultrathin silicon oxide layer located between the SiC substrate and quasifreestanding graphene by considering the silicon bonding states in the Si 2p core-level spectrum. Ideally, during oxygen intercalation the carbon atoms released from the SiC are oxidized to volatile carbon monoxide or carbon dioxide, and oxidation of the Si atoms results in the formation of an ultrathin SiO_2 layer without the formation of amorphous carbon [39]. Furthermore, Oida *et al.* revealed from their data an ~3 Å thick SiO_2 layer on the SiC substrate [39]. Similar C 1s and Si 2p core-level spectra were obtained from our QFMLG sample annealed at 900 °C as shown in Fig. 3(c). The C 1s spectrum of the sample treated in nitrogen atmosphere containing low impurity concentrations of oxygen and water consists of two components. The signal at a binding energy of 283.1 eV (light blue, SiC) originates from carbon atoms of the SiC bulk, whereas the asymmetric component at 284.2 eV (dark blue, G) relates to carbon atoms in the decoupled graphene layer, in agreement with literature reports on oxygen-intercalated graphene [37–42]. The absence of additional components characteristic for the carbon atoms of the buffer layer [22] indicates a complete decoupling of the buffer layer from the SiC substrate. Note that the binding energy of the graphene component is ~0.25 eV lower as compared to graphite [64], indicating a p-type doping of the QFMLG in agreement with previous observations [41]. Furthermore, there are no additional components detectable in the C 1s spectrum which could be attributed to covalent bonds of C atoms in the QFMLG to oxygen, which would be expected at binding energies $\gtrsim$286 eV [65]. In the corresponding Si 2p core-level spectra the shoulder at ~103 eV is attributed to silicon in the oxidation state +4 [66]. Compared to the measurement in normal emission (0°), the Si^{+4} signal is significantly larger in the spectrum acquired under 60° emission angle. Due to the shallower emission of the photoelectrons, the effective sampling depth is reduced in the latter case, giving rise to an enhanced surface sensitivity. The Si 2p as well as the survey spectra (see Fig. S1 of Supplemental Material [44]) confirm the formation of a SiO_2 layer at the graphene-substrate interface. It is worth mentioning that no nitrogen (binding energy ~400 eV) could be detected in the survey spectra.

Moreover, the Raman data in Fig. 1(a) as well as in Fig. 3(a) unambiguously demonstrate a significant decrease, but no total elimination of all defect densities inside the graphene crystal lattice. This clearly reveals the opposite behavior of graphene etching [54], where an increase of the defect density is observed with proceeding etching [54]. However, the remaining D peak in the Raman spectrum after annealing at 900 °C does not allow excluding graphene etching to occur during buffer layer intercalation. It is important to note that long annealing times in oxygen-containing atmosphere rather induces etching effects, while hydrogen atoms from water-containing atmosphere are probably bonded to the graphene lattice, leading to a slightly increased sp^3-bond

content within the graphene lattice as demonstrated by Bom *et al.* [42]. However, they have shown that the combination of both oxygen and water molecules as intercalation agent has significantly improved the chemical reactivity to decouple the buffer layer from the SiC surface, which finally avoids the introduction of additional lattice defects within graphene [42]. Hence, we expect a similar behavior considering the oxygen and water impurities within the nitrogen atmosphere as shown in our experiments. Besides the defect densities, the appearance and evolution of strain and doping in QFMLG were also considered using the strain-doping trajectory as shown in Fig. 3(d) [58]. The Grüneisen parameters γ as determined by Androulidakis *et al.* were used for strain assessment [67]. A slight but steady progress of carrier densities from 5×10^{12} to $1 \times 10^{13}\,\mathrm{cm}^{-2}$ (p-type) was observed between 600 and 900 °C and is confirmed by an average G peak width of $(16.2 \pm 3.9)\,\mathrm{cm}^{-1}$ at 600 °C, $(12.2 \pm 1.3)\,\mathrm{cm}^{-1}$ at 700 °C, $(13.2 \pm 1.5)\,\mathrm{cm}^{-1}$ at 800 °C, and $(13.1 \pm 1.9)\,\mathrm{cm}^{-1}$ at 900 °C [60,68], whereas the standard deviation indicates local fluctuations in the carrier density distribution in QFMLG. Additionally, the electronic transport on the intercalated sample with a size of (5 × 5) mm² was investigated using the van der Pauw method at room temperature. The measurements have revealed an improved charge-carrier mobility of about $\mu \sim 620\,\mathrm{cm}^2\,\mathrm{V}^{-1}\,\mathrm{s}^{-1}$ as compared to Ostler *et al.* ($\mu \sim 420\,\mathrm{cm}^2\,\mathrm{V}^{-1}\,\mathrm{s}^{-1}$) [41] as well as p-type doping in QFMLG of up to $p \sim 2.9 \times 10^{13}\,\mathrm{cm}^{-2}$ as determined by Raman spectroscopy and XPS. Furthermore, Figs. 3(b) and 3(d) show the strain evolution, revealing an elevated tensile strain (0.2%) in graphene at 500 °C which subsequently decreases slightly below 0.2% at 600 and 700 °C. Since no G peak splitting [69,70] occurred during the intercalation process, we suggest that biaxial strain levels exist in the graphene lattice. However, the strain level estimated for graphene annealed at 500 °C might be considered as erroneous due to the fact that high defect densities also affect the G peak position [53]. In addition, the Grüneisen parameter γ as a measure for strain assessment is adaptable for pristine graphene, but has, so far, not been proven for graphene containing high defect densities. The tensile strain level in QFMLG increases again at 900 °C significantly above 0.2%, probably caused by high annealing temperatures but has not been further investigated in this context.

IV. SUMMARY

In conclusion, we have investigated the structural transition from a buffer layer to QFMLG by means of confocal Raman spectroscopy. It could be shown that the phonon properties of the buffer layer as well as those of the QFMLG undergo major lattice transformations in the temperature range between 25 and 900 °C. We have observed the transition of the buffer layer into QFMLG around 400 and 500 °C in a nitrogen atmosphere (∼1 bar, 5N purity) containing low impurity concentrations of oxygen and water. High defect densities in graphene appeared at 500 °C, revealing a nanocrystalline regime related to the stage 2 of the amorphization trajectory presumably containing vacancy-type defects and grain boundaries. Continuous annealing up to 900 °C revealed the transition into stage 1 as evidenced by a rapid decrease but no total removal of the defect densities in QFMLG, nonetheless confirming the existence of high-quality graphene. However, high annealing temperatures and the duration of the intercalation process considerably affect the strain level in graphene. Raman spectroscopy proved to be an effective method for providing deeper insights into the mechanism of the intercalation process of the buffer layer and for more precisely controlling of this process.

ACKNOWLEDGMENT

The authors are thankful to W. Dziony, G. Lilienkamp, and W. Daum for the preliminary XPS measurement.

[1] A. K. Geim and K. S. Novoselov, Nat. Mater. **6**, 183 (2007).
[2] J. A. Alexander-Webber, J. Huang, D. K. Maude, T. J. B. M. Janssen, A. Tzalenchuk, V. Antonov, T. Yager, S. Lara-Avila, S. Kubatkin, R. Yakimova, and R. J. Nicholas, Sci. Rep. **6**, 30296 (2016).
[3] K. I. Bolotin, F. Ghahari, M. D. Shulman, H. L. Stormer, and P. Kim, Nature (London) **462**, 196 (2009).
[4] Y. Zhang, Y.-W. Tan, H. L. Stormer, and P. Kim, Nature (London) **438**, 201 (2005).
[5] G. S. Kulkarni, K. Reddy, Z. Zhong, and X. Fan, Nat. Commun. **5**, 4376 (2014).
[6] F. Schwierz, Nat. Nanotechnol. **5**, 487 (2010).
[7] J. Schurr, C.-C. Kalmbach, F. J. Ahlers, F. Hohls, M. Kruskopf, A. Müller, K. Pierz, T. Bergsten, and R. J. Haug, Phys. Rev. B **96**, 155443 (2017).
[8] H. Choi, J. S. Choi, J.-S. Kim, J.-H. Choe, K. H. Chung, J.-W. Shin, J. T. Kim, D.-H. Youn, K.-C. Kim, J.-I. Lee, S.-Y. Choi, P. Kim, C.-G. Choi, and Y.-J. Yu, Small **10**, 3685 (2014).
[9] A. Tzalenchuk, S. Lara-Avila, A. Kalaboukhov, S. Paolillo, M. Syväjärvi, R. Yakimova, O. Kazakova, T. J. B. M. Janssen, V. Fal'ko, and S. Kubatkin, Nat. Nanotechnol. **5**, 186 (2010).
[10] S. Lee, K. Lee, and Z. Zhong, Nano Lett. **10**, 4702 (2010).
[11] Y. Lee, S. Bae, H. Jang, S. Jang, S.-E. Zhu, S. H. Sim, Y. I. Song, B. H. Hong, and J.-H. Ahn, Nano Lett. **10**, 490 (2010).
[12] E. S. Polsen, D. Q. McNerny, B. Viswanath, S. W. Pattinson, and A. John Hart, Sci. Rep. **5**, 10257 (2015).
[13] S. Bae, H. Kim, Y. Lee, X. Xu, J.-S. Park, Y. Zheng, J. Balakrishnan, T. Lei, H. Ri Kim, Y. I. Song, Y.-J. Kim, K. S. Kim, B. Özyilmaz, J.-H. Ahn, B. H. Hong, and S. Iijima, Nat. Nanotechnol. **5**, 574 (2010).
[14] A. Turchanin, Ann. Phys. **529**, 1700168 (2017).
[15] A. Turchanin, A. Beyer, C. T. Nottbohm, X. Zhang, R. Stosch, A. Sologubenko, J. Mayer, P. Hinze, T. Weimann, and A. Gölzhäuser, Adv. Mater. **21**, 1233 (2009).
[16] D. G. Matei, N.-E. Weber, S. Kurasch, S. Wundrack, M. Woszczyna, M. Grothe, T. Weimann, F. Ahlers, R. Stosch, U. Kaiser, and A. Turchanin, Adv. Mater. **25**, 4146 (2013).

[17] M. Woszczyna, A. Winter, M. Grothe, A. Willunat, S. Wundrack, R. Stosch, T. Weimann, F. Ahlers, and A. Turchanin, Adv. Mater. **26**, 4831 (2014).

[18] M. Kruskopf, D. Momeni Pakdehi, K. Pierz, S. Wundrack, R. Stosch, T. Dziomba, M. Götz, J. Baringhaus, J. Aprojanz, C. Tegenkamp, J. Lidzba, T. Seyller, F. Hohls, F. J. Ahlers, and H. W. Schumacher, 2D Mater. **3**, 041002 (2016).

[19] C. Berger, Z. Song, T. Li, X. Li, A. Y. Ogbazghi, R. Feng, Z. Dai, A. N. Marchenkov, E. H. Conrad, P. N. First, and W. A. de Heer, J. Phys. Chem. B **108**, 19912 (2004).

[20] K. V. Emtsev, A. Bostwick, K. Horn, J. Jobst, G. L. Kellogg, L. Ley, J. L. McChesney, T. Ohta, S. A. Reshanov, J. Röhrl, E. Rotenberg, A. K. Schmid, D. Waldmann, H. B. Weber, and T. Seyller, Nat. Mater. **8**, 203 (2009).

[21] M. Kruskopf, K. Pierz, S. Wundrack, R. Stosch, T. Dziomba, C.-C. Kalmbach, A. Müller, J. Baringhaus, C. Tegenkamp, F. J. Ahlers, and H. W. Schumacher, J. Phys.: Condens. Matter **27**, 185303 (2015).

[22] K. V. Emtsev, F. Speck, T. Seyller, L. Ley, and J. D. Riley, Phys. Rev. B **77**, 155303 (2008).

[23] J. Ristein, S. Mammadov, and T. Seyller, Phys. Rev. Lett. **108**, 246104 (2012).

[24] S. Kopylov, A. Tzalenchuk, S. Kubatkin, and V. I. Fal'ko, Appl. Phys. Lett. **97**, 112109 (2010).

[25] E. Pallecchi, F. Lafont, V. Cavaliere, F. Schopfer, D. Mailly, W. Poirier, and A. Ouerghi, Sci. Rep. **4**, 4558 (2015).

[26] F. Speck, J. Jobst, F. Fromm, M. Ostler, D. Waldmann, M. Hundhausen, H. B. Weber, and T. Seyller, Appl. Phys. Lett. **99**, 122106 (2011).

[27] D. Yoon, Y.-W. Son, and H. Cheong, Nano Lett. **11**, 3227 (2011).

[28] S. Linas, Y. Magnin, B. Poinsot, O. Boisron, G. D. Förster, V. Martinez, R. Fulcrand, F. Tournus, V. Dupuis, F. Rabilloud, L. Bardotti, Z. Han, D. Kalita, V. Bouchiat, and F. Calvo, Phys. Rev. B **91**, 075426 (2015).

[29] J. Robinson, C. Puls, N. Staley, J. Stitt, M. Fanton, K. Emtsev, T. Seyller, and Y. Liu, Nano Lett. **9**, 964 (2009).

[30] D. S. Lee, C. Riedl, B. Krauss, K. von Klitzing, U. Starke, and J. H. Smet, Nano Lett. **8**, 4320 (2008).

[31] J. Röhrl, M. Hundhausen, K. V. Emtsev, T. Seyller, R. Graupner, and L. Ley, Appl. Phys. Lett. **92**, 201918 (2008).

[32] Y.-P. Lin, Y. Ksari, and J.-M. Themlin, Nano Res. **8**, 839 (2015).

[33] C. Riedl, C. Coletti, T. Iwasaki, A. A. Zakharov, and U. Starke, Phys. Rev. Lett. **103**, 246804 (2009).

[34] I. Gierz, T. Suzuki, R. T. Weitz, D. S. Lee, B. Krauss, C. Riedl, U. Starke, H. Höchst, J. H. Smet, C. R. Ast, and K. Kern, Phys. Rev. B **81**, 235408 (2010).

[35] C. Virojanadara, A. A. Zakharov, S. Watcharinyanon, R. Yakimova, and L. I. Johansson, New J. Phys. **12**, 125015 (2010).

[36] S. Mammadov, J. Ristein, R. J. Koch, M. Ostler, C. Raidel, M. Wanke, R. Vasiliauskas, R. Yakimova, and T. Seyller, 2D Mater. **1**, 035003 (2014).

[37] G. Kowalski, M. Tokarczyk, P. Dąbrowski, P. Ciepielewski, M. Możdżonek, W. Strupiński, and J. M. Baranowski, J. Appl. Phys. **117**, 105301 (2015).

[38] M. Ostler, R. J. Koch, F. Speck, F. Fromm, H. Vita, M. Hundhausen, K. Horn, and T. Seyller, Mater. Sci. Forum **717-720**, 649 (2012).

[39] S. Oida, F. R. McFeely, J. B. Hannon, R. M. Tromp, M. Copel, Z. Chen, Y. Sun, D. B. Farmer, and J. Yurkas, Phys. Rev. B **82**, 041411(R) (2010).

[40] M. H. Oliveira, T. Schumann, F. Fromm, R. Koch, M. Ostler, M. Ramsteiner, T. Seyller, J. M. J. Lopes, and H. Riechert, Carbon **52**, 83 (2013).

[41] M. Ostler, F. Fromm, R. J. Koch, P. Wehrfritz, F. Speck, H. Vita, S. Böttcher, K. Horn, and T. Seyller, Carbon **70**, 258 (2014).

[42] N. M. Bom, M. H. Oliveira, G. V. Soares, C. Radtke, J. M. J. Lopes, and H. Riechert, Carbon **78**, 298 (2014).

[43] D. Momeni Pakdehi, J. Aprojanz, A. Sinterhauf, K. Pierz, M. Kruskopf, P. Willke, J. Baringhaus, J. P. Stöckmann, G. A. Traeger, F. Hohls, C. Tegenkamp, M. Wenderoth, F. J. Ahlers, and H. W. Schumacher, ACS Appl. Mater. Interfaces **10**, 6039 (2018).

[44] See Supplemental Material at http://link.aps.org/supplemental/10.1103/PhysRevB.99.045443 for further details about Raman mapping evaluation in terms of peak position and peak width using nonlinear curve-fitting.

[45] F. Fromm, M. Oliveira, A. Molina-Sánchez, M. Hundhausen, J. Lopes, H. Riechert, L. Wirtz, and T. Seyller, New J. Phys. **15**, 043031 (2013).

[46] A. C. Ferrari and D. M. Basko, Nat. Nanotechnol. **8**, 235 (2013).

[47] L. Cançado, A. Jorio, E. Ferreira, F. Stavale, C. Achete, R. Capaz, M. Moutinho, A. Lombardo, T. Kulmala, and A. Ferrari, Nano Lett. **11**, 3190 (2011).

[48] A. Eckmann, A. Felten, A. Mishchenko, L. Britnell, R. Krupke, K. S. Novoselov, and C. Casiraghi, Nano Lett. **12**, 3925 (2012).

[49] L. G. Cançado, K. Takai, T. Enoki, M. Endo, Y. A. Kim, H. Mizusaki, A. Jorio, L. N. Coelho, R. Magalhães-Paniago, and M. A. Pimenta, Appl. Phys. Lett. **88**, 163106 (2006).

[50] R. Lv, Q. Li, A. R. Botello-Méndez, T. Hayashi, B. Wang, A. Berkdemir, Q. Hao, A. L. Elías, R. Cruz-Silva, H. R. Gutiérrez, Y. A. Kim, H. Muramatsu, J. Zhu, M. Endo, H. Terrones, J.-C. Charlier, M. Pan, and M. Terrones, Sci. Rep. **2**, 586 (2012).

[51] L. Zhao, R. He, K. T. Rim, T. Schiros, K. S. Kim, H. Zhou, C. Gutierrez, S. P. Chockalingam, C. J. Arguello, L. Palova, D. Nordlund, M. S. Hybertsen, D. R. Reichman, T. F. Heinz, P. Kim, A. Pinczuk, G. W. Flynn, and A. N. Pasupathy, Science **333**, 999 (2011).

[52] A. C. Ferrari and J. Robertson, Phys. Rev. B **64**, 075414 (2001).

[53] A. C. Ferrari and J. Robertson, Phys. Rev. B **61**, 14095 (2000).

[54] I. Childres, L. A. Jauregui, J. Tian, and Y. P. Chen, New J. Phys. **13**, 025008 (2011).

[55] J. Moser, H. Tao, S. Roche, F. Alsina, C. M. Sotomayor Torres, and A. Bachtold, Phys. Rev. B **81**, 205445 (2010).

[56] L. Liu, S. Ryu, M. R. Tomasik, E. Stolyarova, N. Jung, M. S. Hybertsen, M. L. Steigerwald, L. E. Brus, and G. W. Flynn, Nano Lett. **8**, 1965 (2008).

[57] R. Beams, L. Gustavo Cançado, and L. Novotny, J. Phys.: Condens. Matter **27**, 083002 (2015).

[58] J. E. Lee, G. Ahn, J. Shim, Y. S. Lee, and S. Ryu, Nat. Commun. **3**, 1024 (2012).

[59] D. Graf, F. Molitor, K. Ensslin, C. Stampfer, A. Jungen, C. Hierold, and L. Wirtz, Nano Lett. **7**, 238 (2007).

[60] A. Das, S. Pisana, B. Chakraborty, S. Piscanec, S. K. Saha, U. V. Waghmare, K. S. Novoselov, H. R. Krishnamurthy, A. K. Geim, A. C. Ferrari, and A. K. Sood, Nat. Nanotechnol. **3**, 210 (2008).

[61] E. H. Martins Ferreira, M. V. O. Moutinho, F. Stavale, M. M. Lucchese, R. B. Capaz, C. A. Achete, and A. Jorio, Phys. Rev. B **82**, 125429 (2010).

[62] J. A. Robinson, M. Hollander, M. LaBella, K. A. Trumbull, R. Cavalero, and D. W. Snyder, Nano Lett. **11**, 3875 (2011).

[63] A. Eckmann, A. Felten, I. Verzhbitskiy, R. Davey, and C. Casiraghi, Phys. Rev. B **88**, 035426 (2013).

[64] G. K. Wertheim, P. M. T. M. Van Attekum, and S. Basu, Solid State Commun. **33**, 1127 (1980).

[65] G. Beamson and D. Briggs, *High Resolution XPS of Organic Polymers* (John Wiley & Sons, Chichester, 1992).

[66] N. Sieber, T. Seyller, R. Graupner, L. Ley, R. Mikalo, P. Hoffmann, D. R. Batchelor, and D. Schmeißer, Appl. Surf. Sci. **184**, 278 (2001).

[67] C. Androulidakis, E. N. Koukaras, J. Parthenios, G. Kalosakas, K. Papagelis, and C. Galiotis, Sci. Rep. **5**, 18219 (2015).

[68] M. Bruna, A. K. Ott, M. Ijäs, D. Yoon, U. Sassi, and A. C. Ferrari, ACS Nano **8**, 7432 (2014).

[69] T. M. G. Mohiuddin, A. Lombardo, R. R. Nair, A. Bonetti, G. Savini, R. Jalil, N. Bonini, D. M. Basko, C. Galiotis, N. Marzari, K. S. Novoselov, A. K. Geim, and A. C. Ferrari, Phys. Rev. B **79**, 205433 (2009).

[70] N. S. Mueller, S. Heeg, M. P. Alvarez, P. Kusch, S. Wasserroth, N. Clark, F. Schedin, J. Parthenios, K. Papagelis, C. Galiotis, M. Kalbáč, A. Vijayaraghavan, U. Huebner, R. Gorbachev, O. Frank, and S. Reich, 2D Mater. **5**, 015016 (2017).